RSC Advances

PAPER

Cite this: *RSC Adv.*, 2020, **10**, 30756

One-step production of N–O–P–S co-doped porous carbon from bean worms for supercapacitors with high performance†

Zhentao Bian,*[ab] Chunjie Wu,[a] Chenglong Yuan,[a] Ying Wang,[a] Guangzhen Zhao,[a] Hongyan Wang,[a] Yong Xie,[ab] Cong Wang,[a] Guang Zhu[a] and Chong Chen*[a]

In recent years, multi-heteroatom-doped hierarchical porous carbons (HPCs) derived from natural potential precursors and synthesized in a simple, efficient and environmentally friendly manner have received extensive attention in many critical technology applications. Herein, bean worms (BWs), a pest in bean fields, were innovatively employed as a precursor *via* a one-step method to prepare N–O–P–S co-doped porous carbon materials. The pore structure and surface elemental composition of carbon can be modified by adjusting KOH dosage, exhibiting a high surface area (S_{BET}) of 1967.1 m^2 g^{-1} together with many surface functional groups. The BW-based electrodes for supercapacitors were shown to have a good capacitance of up to 371.8 F g^{-1} in 6 M KOH electrolyte at 0.1 A g^{-1}, and good rate properties with 190 F g^{-1} at a high current density of 10 A g^{-1}. Furthermore, a symmetric supercapacitor based on the optimal carbon material ($BWPC_{1/3}$) was also assembled with a wide voltage window of 2.0 V, demonstrating satisfactory energy density (27.5 W h kg^{-1} at 200 W kg^{-1}) and electrochemical cycling stability (97.1% retention at 10 A g^{-1} over 10 000 charge/discharge cycles). The facile strategy proposed in this work provides an attractive way to achieve high-efficiency and scalable production of biomass-derived HPCs for energy storage.

Received 6th July 2020
Accepted 11th August 2020

DOI: 10.1039/d0ra05870j

rsc.li/rsc-advances

1 Introduction

The huge demand for and depletion of non-renewable fossil energy have resulted in a global energy crisis over recent years.[1] To deal with these urgent issues, the development of reliable and cost-effective electrochemical energy storage systems has become increasingly prominent. Supercapacitors (SC), as one of the most promising energy storage devices, provide an opportunity to address this challenge and are becoming more prevalent due to their multiple advantages, such as quick recharging, high specific power density, and long cycling life.[2,3]

Typically, carbon materials, including carbon nanotubes,[4] graphene,[5] carbon nanosheets,[6,7] activated carbon,[8] metal–organic frameworks (MOFs)[9] and carbon nanofibers[10] are often used as electrical double-layer capacitor (EDLC) electrodes. Nevertheless, there are a number of issues that affect the commercial application of these materials, including high cost, poor electrical conductivity, and low power density. Recent studies found that electrode materials with three-dimensional hierarchical porous nanostructures, including micropores, mesopores and macrospores are more suitable for energy storage.[11] As a result, hierarchically porous carbon material has been deeply explored for this purpose with considerable progress achieved.[12]

Energy storage capacity of carbon-based supercapacitors is dependent on the adsorption of electrolyte ions or reversible redox reaction at the interfaces of electrode and electrolyte. A large number of micropores (less than 2 nm in diameter) in the carbon material is considered to be critically important for increasing energy density by providing abundant accessible surface area as well as active sites. However, electrolyte ions cannot effectively transport into interior pores in micropores dominated carbon, leading to inferior power performance of electrode materials. It is generally believed that the mesopores (2–50 nm), especially narrow mesopores, can provide a short electron and ion transport pathway, enhancing the utilization ratio of the micropores.[13,14] Besides, macropores (>50 nm) can act as a fast buffering reservoir to store more electrolyte ions. Hence, the rational design of pore structures with abundant appropriate micropores, macro- and mesopores of carbon materials is of great significance to their capacitive performances and rate capability.

Introducing heteroatoms into carbon network is another productive way to attain excellent electrochemical

[a]Anhui Key Laboratory of Spin Electron and Nanomaterials (Cultivating Base), School of Chemistry and Chemical Engineering, Suzhou University, Suzhou 234000, PR China. E-mail: chongchen_li@163.com

[b]Institute of Fine Chemical Products Development, Suzhou University, Suzhou 234000, PR China

† Electronic supplementary information (ESI) available. See DOI: 10.1039/d0ra05870j

performances without change the original orientation structure.[15,16] Research results indicate that the present of oxygen can significantly enhance the wettability to electrolyte, improving the micropores accessibility of electrolyte ions, offering more active sites for reversible redox reactions, and ensuring superior capacitive properties of carbon material.[17] Moreover, both conductivity and wettability of carbon materials can be substantially promoted by introducing nitrogen into carbon skeleton, leading to better electrochemical performance.[18] Apart from N and O, another class of functional materials, including S, B and P, also possessing physio/chemical properties suitable for superior cell outputs.[6,19] In comparison to mono-heteroatom doping, multi-heteroatom doping can further enhance the overall performances of the carbon materials because of the synergetic interaction between different heteroatoms.[20–22] Therefore, enormous efforts are devoted to optimizing the electrochemical performance of carbon materials by incorporating multiple heteroatoms into the framework of carbon. Nevertheless, to our knowledge, S/P/N/O co-doped carbon has seldom been reported.

To fabricate HPCs with high surface area, various activating agents, including KOH, NaOH, $ZnCl_2$, H_3PO_4 and $CaCl_2$ have been adopted.[23,24] Among them, KOH exhibits many advantages, especially on forming uniform pore structure and large S_{BET}, which was reported as among the most promising activating agent for producing porous carbon materials.[18,25,26] Moreover, this process is also suitable for large-scale production of carbon materials. Generally, chemical activation of carbon materials by KOH can be divided into one-pot process and hydrothermal/pre-carbonization plus KOH activation strategies (two-step mechanism).[27–30] The former takes shorter time and produces a high yield, but usually produces an unsatisfactory broad pore size distribution (PSD), resulting in reduced capacitance.[13] The drawback of the later, however, is that the process is sophisticated and time-consuming, and a large amount of KOH was used. Moreover, the activation conditions and precursors used significantly affect the structural properties and surface functionalities of KOH-activated carbons.[14] Thus, it is highly necessary to choose an appropriate raw material and develop a facile KOH synthesis strategy to prepare the carbon materials.

As sustainable and renewable biomass materials, legumes and byproducts of legumes are rich in plant proteins,[31] which is mainly composed of complete protein with elements of C, S, O and N. Hence, legumes-derived HPCs have been extensively applied as highly conductive materials for supercapacitor.[11,32–36] For instance, Yao *et al.*[11] reported *Bradyrhizobium japonicum*-derived 3D hierarchical porous carbon with high N content, the as-prepared material was of large S_{BET}, unique three-dimensional hierarchical porosity and also excellent electrochemical performance. Lin *et al.*[33] synthesized nitrogen-doped HPCs by using soybean as starting material, and a high energy density was obtained. Bean worm (BW), a widely distributed invertebrate in China, living on soybean, acacia, robinia and honeysuckle. In China, bean worms have been bred and developed into an industry since the last century and a large number of bean worms are marketed all over China annually. Furthermore, BWs are ideal plant protein resources (about 63.2% of the dry weight).[37] That is to say, it contains an abundance of carbon, oxygen, nitrogen, and sulfur. Thus, BW is expected to provide a new insight for the use of legumes-derived biomass to synthesis multi-heteroatom-doped materials as an effective candidate of electrode active materials for practical supercapacitors.

Here, we report our use of a very simple, one-step carbonization process (Fig. 1) to produce HPCs with abundant functional groups, using the bean worm as a novel carbon source. The meanings of our work are as follow: (1) the present research can deepen our understanding of the doping mechanism of heteroatoms and the parameters for activation in relation to improving electrochemical properties; (2) the fabrication route is facile, less energy consumption and easy handling, which is suitable for large-scale production of carbon materials; (3) the as-obtained carbon materials exhibits large S_{BET}, hierarchical pore architecture, high content of N, O, P and S heteroatoms. Also, a remarkable specific capacitance of 371.8 F g^{-1} is obtained. These findings demonstrate that bean worm-derived HPCs will be promising electrode materials for sustainable energy applications.

2 Experimental details

2.1 Materials

Bean worms were collected from local farm of Suzhou, Anhui Province of China. Potassium hydroxide (wt% > 85%, KOH), hydrochloric acid (37 wt%, HCl), and ethanol were purchased from Aladdin Chemistry Co., Ltd (China). All chemicals were analytical grade.

2.2 Preparation of bean worms derived carbon materials

BWs were soaked and cleaned with distilled water, dried at 110 °C for 24 h, and then cut into pieces with scissors. The yellow BW slices were mixed with KOH in 250 ml deionized water, and then vigorously stirred for 36 h. After that, the KOH attached BWs were dried in an oven at 120 °C for 24 h and then heated to 700 °C with a rate of 5 °C min^{-1} in N_2 atmosphere, held there for 2 h. The collected samples were then rinsed in diluted HCl and deionized water, and finally dried at 120 °C overnight. When different contents of KOH were used, the carbonization products were denoted as $BWPC_{1/x}$, where x are 2, 3 and 4 for all BW-derived HPCs. For instance, $BWPC_{1/2}$ represents a carbon material, in which the mass ratio of KOH to BW was 1 : 2. For comparison, a carbon named as BWC was manufactured under identical conditions in the absence of KOH.

2.3 Material characterization

Scanning electron microscopy (SEM, Hitachi S-2600N), transmission electron microscope and high-resolution transmission electron microscopic (TEM and HRTEM, JEOL JEM-2100F) were applied to observe the microstructures. Pore structure properties were analyzed by N_2 adsorption and desorption isotherms at 77 K (Micromeritics ASAP 2460, USA). The S_{BET} and PSD were determined by the Brunauer–Emmett–Teller (BET) method and

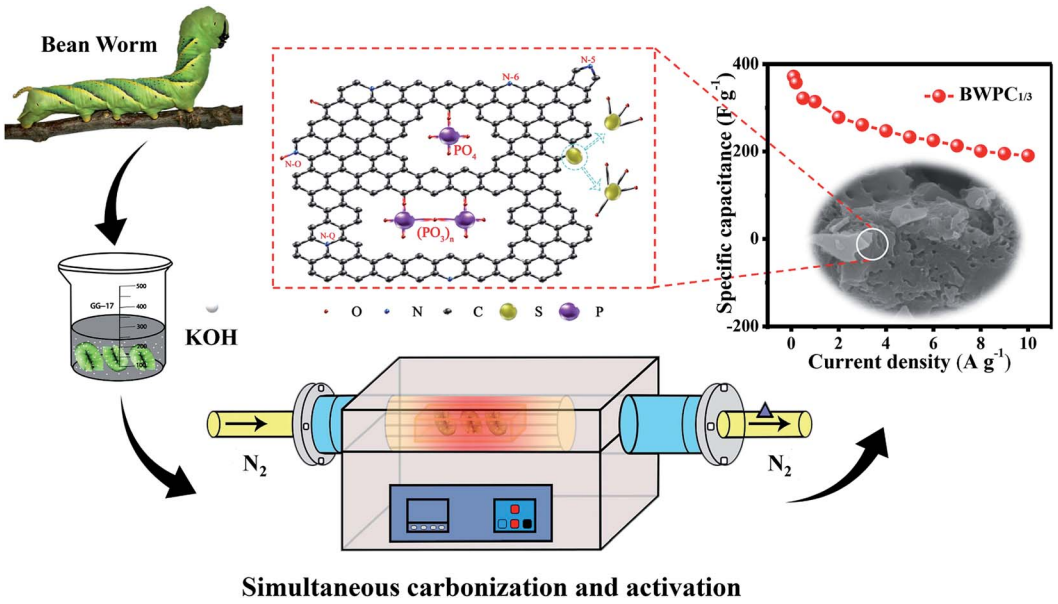

Fig. 1 Schematic diagram of the preparation of bean worm derived carbon.

the density functional theory (DFT) model. The defective nature of the materials was measured by Raman spectrometer (Thermo Fisher), while the chemical composition was conducted by an X-ray photoelectron spectrometer (XPS, 250Xi, Thermo Fisher Escalab, USA). The crystalline and phase structure for all BWPCs were measured *via* X-ray diffraction (XRD, Smartlab 9 kW, Japan) from 10–80° at a scan rate of 5° min^{-1}.

2.4 Electrochemical measurement

The electrochemical measurements for all products were conducted on a CHI760D electrochemical workstation. To prepare the working electrode, the active material, polytetrafluoroethylene (PTFE), and acetylene black were mixed with a ratio of 80 : 15 : 5 by weight. The slurry was then coated onto one side of a nickel foam (1 cm × 1 cm) and dried at 85 °C for 24 h. The

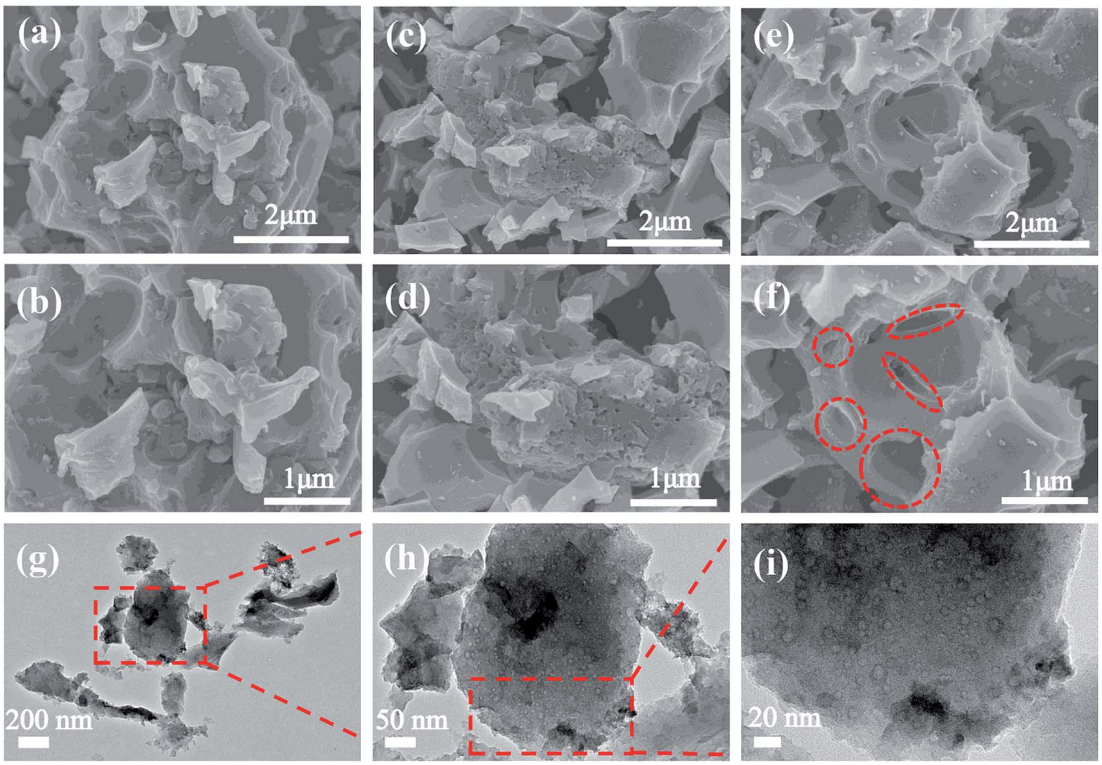

Fig. 2 SEM images of (a and b) $BWPC_{1/4}$, (c and d) $BWPC_{1/3}$, (e and f) $BWPC_{1/2}$ and (g–i) TEM images of $BWPC_{1/3}$.

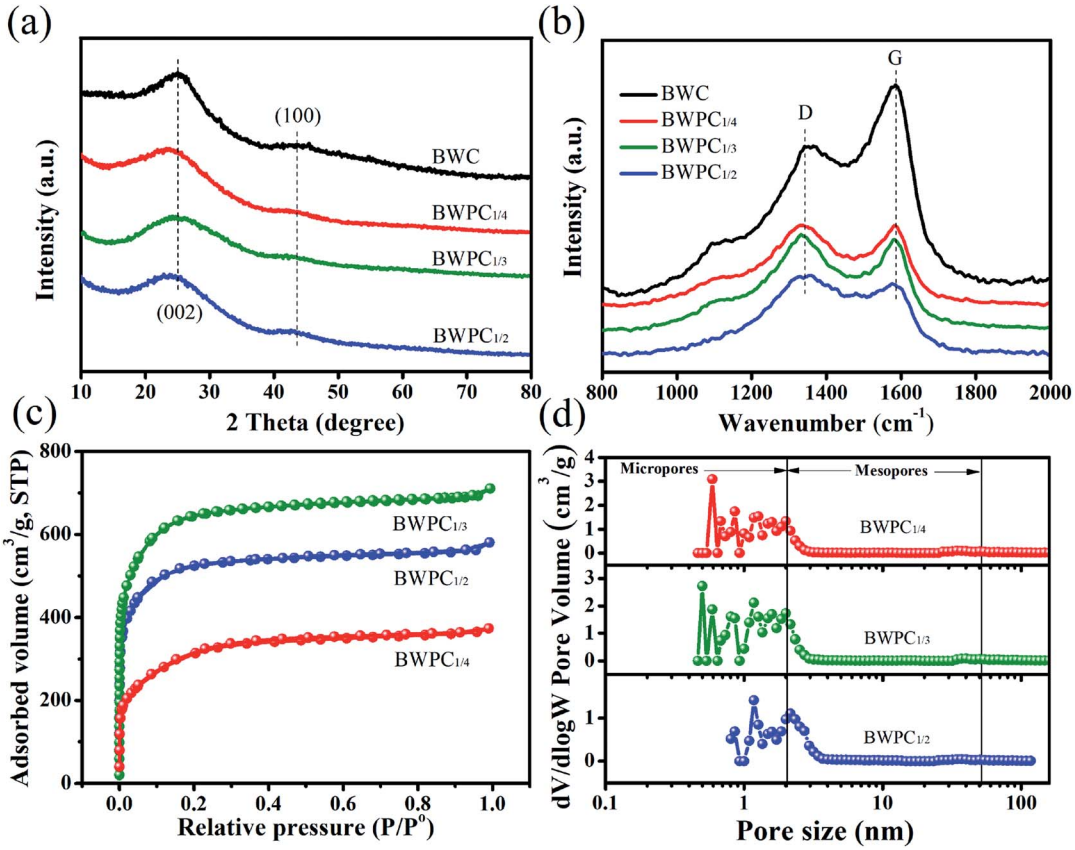

Fig. 3 (a) XRD patterns, (b) Raman spectra, (c) nitrogen adsorption–desorption isotherms, and (d) PSD of $BWPC_{1/4}$, $BWPC_{1/3}$, and $BWPC_{1/2}$.

load of the active material on each nickel foam was about 2 mg cm^{-2}. A platinum wire and a Hg/HgO electrode served as counter and reference electrodes in a three-electrode system, respectively. Electrochemical impedance spectroscopy (EIS) was tested in a frequency domain of 0.01–10^5 Hz with an amplitude of 5 mV. Galvanostatic charge/discharge (GCD), cyclic voltammetry (CV) and EIS measurements were conducted in 6 M KOH solution.

The specific capacitance (C_s, F g^{-1}) was calculated according to the GCD tests depended on formula (1):

$$C_s = (I \times \Delta t)/(m \times \Delta V) \quad (1)$$

The symmetrical coin-type supercapacitors were assembled by two nearly identical round (diameter ~ 12 mm) $BWPC_{1/3}$ based electrodes using glassy fiber as separator, 6 M KOH and 1 M Na_2SO_4 as electrolytes. The electrodes with the active material mass loading of ~2 mg cm^{-2} were prepared using the same method mentioned above. The gravimetric capacitance (C_g, F g^{-1}) of the total device was calculated with the following equation:

$$C_g = (I \times \Delta t)/(M \times \Delta V) \quad (2)$$

The energy density (E, W h kg^{-1}) and power density (P, W kg^{-1}) were calculated based on the following formulas:

$$E = 0.5C_g \times \Delta V^2/3.6 \quad (3)$$

$$P = 3600E/\Delta t \quad (4)$$

where, the discharge current is defined as I (A), Δt (s) means the discharge time, ΔV (V) signifies the potential window, m (g) is the mass of the active material in the working electrode, M (g) is the total mass of the active materials on both electrodes.

Table 1 Pore structure parameters of BW-derived samples

Sample	S_{BET} (m^2 g^{-1})	S_{micro} (m^2 g^{-1})	V_{total} (cm^3 g^{-1})	V_{micro} (cm^3 g^{-1})	V_{micro}/V_{total} (%)	D_{ave} (nm)
BWC	0.0147	—	0.003	—	—	—
$BWPC_{1/4}$	1043.3	264.6	0.56	0.14	25.0	2.04
$BWPC_{1/3}$	1967.1	1216.2	1.08	0.76	70.12	2.18
$BWPC_{1/2}$	1568.8	1115.1	0.87	0.53	61.11	2.25

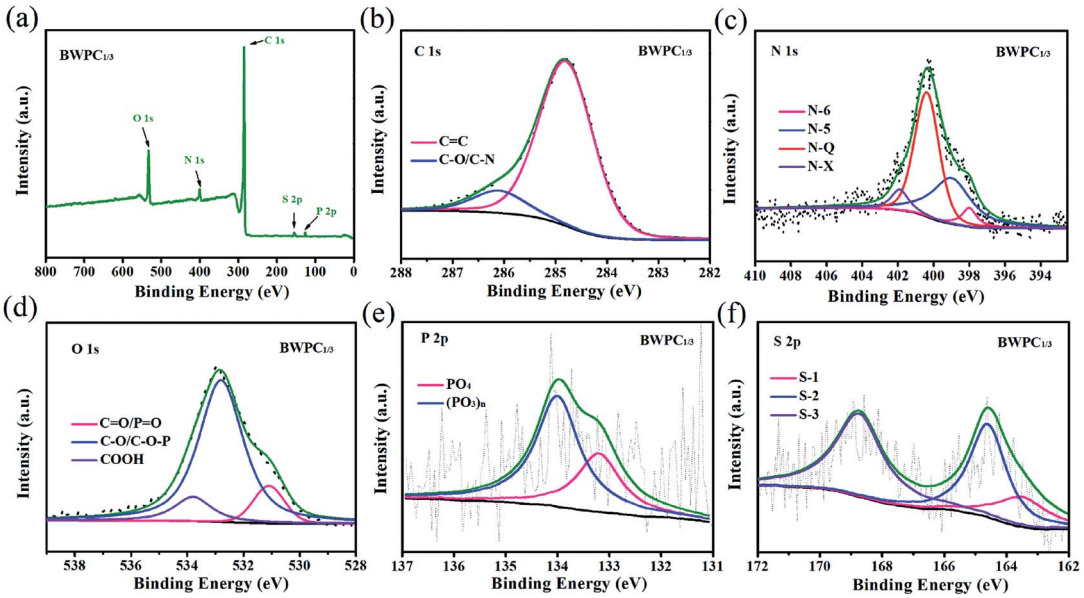

Fig. 4 XPS spectra (a) and deconvolved C 1s spectra (b), N 1s spectra (c) O 1s spectra (d), P 2p spectra (e) and S 2p (f) of $BWPC_{1/3}$.

Table 2 Calculated results from XPS and Raman spectra

	XPS (at%)					
Sample	C	N	O	P	S	I_D/I_G
BWC	82.81	5.63	10.58	0.61	0.38	0.83
$BWPC_{1/4}$	83.41	4.67	11.42	0.22	0.28	1.00
$BWPC_{1/3}$	82.34	4.36	12.86	0.21	0.23	1.10
$BWPC_{1/2}$	81.28	4.12	14.27	0.17	0.16	1.05

3 Results and discussion

The bean worms used in this experiment originated from the local farm of Suzhou, China. Fig. 1 shows the schematic diagram of the preparation of bean worm derived carbon. Initially, bean worms were washed and dried at 110 °C. Subsequently, the obtained material was soaked in KOH solution to guarantee that adequate K^+ and OH^- ions adsorbed to the material. After drying, abundant KOH particles were embedded in the bulk and deposited on the surface of carbon. The reaction between biomass and KOH is mostly described as follows:[38]

$$6KOH + 2C \rightarrow 2K + 3H_2 + 2K_2CO_3 \quad (5)$$

$$K_2CO_3 + C \rightarrow K_2O + 2CO \quad (6)$$

$$K_2CO_3 \rightarrow K_2O + CO_2 \quad (7)$$

$$2K + CO_2 \rightarrow K_2O + CO \quad (8)$$

The microstructure of the biomass precursor and carbon materials obtained under different conditions was characterized by SEM first. For the precursor, complete rectangular block-like structure with smooth surface is observed (Fig. S1a and b†). Fig. S1c–f† show the morphology of BWC, which exhibits block structure with relatively smooth surface. In addition, fragmentized particles and a few open macropores can be found from the block structure. Fig. 2a–f and S1g–l† show the SEM images of BWPCs. As can be seen, the activation with KOH markedly changes the morphology of carbon materials and the large size blocks are broken into smaller ones. Compared with $BWPC_{1/4}$ without obvious pores (demonstrating a weak activation effect because of inadequate KOH activation) and $BWPC_{1/2}$ with many open macropores formed by excessive KOH etching, $BWPC_{1/3}$ exhibits an interconnected porous structure. Fig. 2g–i displays the TEM image of $BWPC_{1/3}$, showing that many nanopores are produced on the walls of the carbon materials. HRTEM images (Fig. S2†) further reveal the hierarchical structure of $BWPC_{1/3}$. Numerous worm-like micropores and mesopores are randomly distributed on the surface of $BWPC_{1/3}$, which can potentially promote the surface area and the pore volume (V_p).[34] The above results suggest that BWPCs with interconnected nanostructure was successfully synthesized *via* the facile one-pot method.

Fig. 3a presents the XRD patterns of the obtained carbons. Two diffraction peaks can be found in BWC and BWPCs at 2θ of 25° and 43.5°, which are assigned the (002) and (100) planes of graphite, respectively.[38] For BWPCs, the (002) peaks become broader and weaker, which might be due to the KOH activation destroys the atomic arrangement, corresponding to the porosity change from nonporous structure to porous structure.[39,40]

Raman spectra of BWC and BWPCs were studied for more structural information. As shown in Fig. 3b, all BW-derived carbons exhibit two distinct peaks at 1350 and 1590 cm^{-1}, referred as the D-band and the G-band, respectively. The D-band reflects the disordered carbon or defective graphitic structures of carbon, whereas the G-band belongs to the ordered graphite structure. The degree of structure defection was assessed by the intensity ratios between the D-band and the

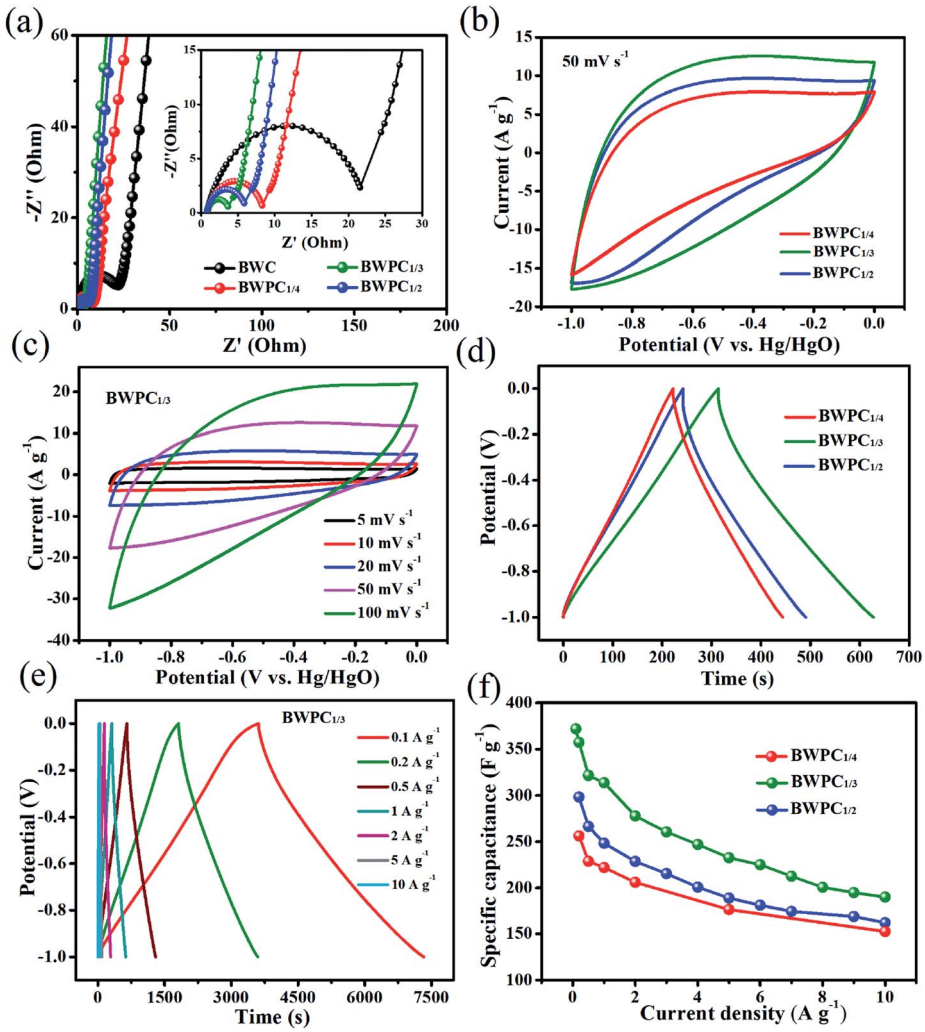

Fig. 5 Electrochemical performances of BW and BWPCs in a three-electrode system using 6 M KOH as the electrolyte: (a) Nyquist plots, (b) CV curves (50 mV s^{-1}), (c) CV curves of $BWPC_{1/3}$ at different scan rates, (d) GCD curves obtained at 1 A g^{-1}, (e) GCD curves of $BWPC_{1/3}$ at 0.1–10 A g^{-1}, (f) the specific capacitances of BWPCs at the current densities from 0.1 to 10 A g^{-1}.

G-band (I_D/I_G). The D/G ratios of $BWPC_{1/4}$, $BWPC_{1/3}$, $BWPC_{1/2}$ and BWC are listed in Table 2. Compared to BWC, BWPCs exhibit higher I_D/I_G value, suggesting defects were introduced in BWPCs due to the oxidation of carbon atoms with KOH.[33,41] Specifically, from $BWPC_{1/3}$ to $BWPC_{1/2}$, the I_D/I_G value decreased, implying the reduced proportion of defects. These results further clarify that excessive usage of KOH causes structural collapse of carbon walls, which destroyed the continuous and interconnected structure of carbon, in accordance with the SEM analysis.

Nitrogen adsorption–desorption measurement for carbons were conducted to determine the development of pore structure, as presented in Fig. 3c and S3.† Obviously, the N_2 adsorption–desorption isotherm of BWC exhibits a type-II

Table 3 Comparison of C_S and S_{BET} of reported similar biomass-derived porous carbons prepared by the KOH activation method

Precursor	S_{BET} (m^2 g^{-1})	C_s (F g^{-1})	Electrolyte	Ref.
Pine nut shells	2093	324 at 0.05 A g^{-1}	6 M KOH	7
Sakura petals	1785.4	268.2 at 0.2 A g^{-1}	6 M KOH	29
Bamboo shoot shells	3250	209 at 0.5 A g^{-1}	6 M KOH	57
Seaweed	1493	207.3 at 0.5 A g^{-1}	1 M KOH	58
Alfalfa flowers	1590.9	350.1 at 0.5 A g^{-1}	6 M KOH	59
Pitaya peel	1872	255 at 1 A g^{-1}	6 M KOH	60
Bean worm	1967.1	371.8 at 0.1 A g^{-1}	6 M KOH	This work

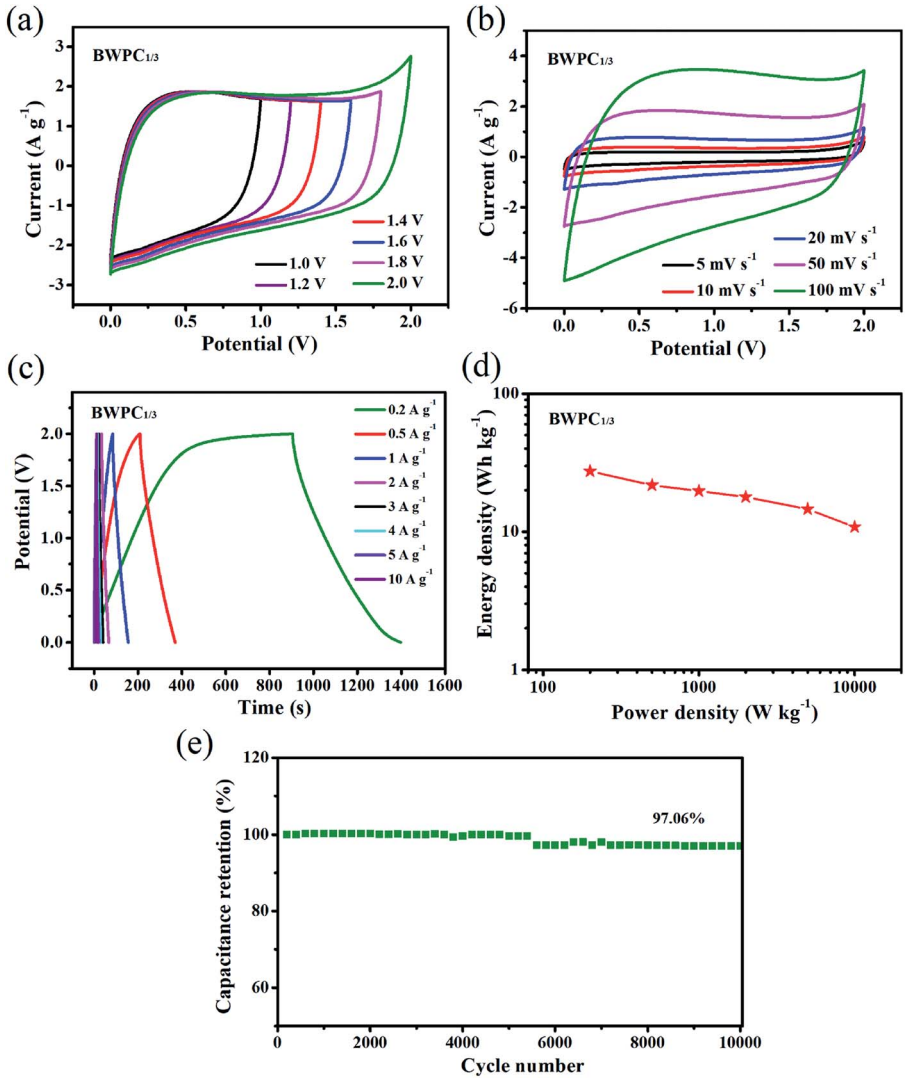

Fig. 6 Electrochemical characteristics of $BWPC_{1/3}$//$BWPC_{1/3}$ symmetric device in 1 M Na_2SO_4 in a two-electrode system: (a) CV curves collected at different operation voltages at 50 mV s^{-1}, (b) CV curves under different sweep speeds, (c) GCD curves collected at different currents, (d) Ragone plot, (e) cycling stability at 10 A g^{-1} for 10 000 cycles.

curve, revealing the non-porous structure. While $BWPC_{1/4}$, $BWPC_{1/3}$ and $BWPC_{1/2}$ reveal a typical-I sorption isotherm characteristic after KOH activation.[42] The drastic rise in volume adsorbed occurs below $P/P_0 = 0.1$, which indicates an abundant presence of micropores. Additionally, the PSD curves presented in Fig. 3d verify that the BWPC material has not only the micropores but also the mesopores.

The corresponding textural parameters of BWC and BWPCs are summarized in Table 1. As expected, the obtained BWC presents an undeveloped pore structure with a rather low V_p (0.003 cm^3 g^{-1}) and S_{BET} (0.0147 m^2 g^{-1}). The porosity of BWPCs was remarkably improved after the activation process by KOH and deeply affected by the BW/KOH mass ratio. The S_{BET} of $BWPC_{1/4}$ and $BWPC_{1/3}$ are 1043.3 and 1967.1 m^2 g^{-1}, whereas the V_p determined using DFT model are 0.56 and 1.08 cm^3 g^{-1}, respectively. However, the V_p and S_{BET} of $BWPC_{1/2}$ are significantly reduced, that are, 0.87 cm^3 g^{-1} and 1568.8 m^2 g^{-1}, which may occur due to the collapse of pores under excessive KOH dosage. Similar results were obtained from the loofah sponge-derived[43] and *Bradyrhizobium japonicum*-derived[11] carbon materials. Hence, $BWPC_{1/3}$ with a well-developed pore structure was expected to demonstrate excellent electrochemical performance.

XPS was applied to analysis the atom binding states and the contents of surface elements in the as-synthesized samples. Fig. 4a and S4a† show the XPS spectrum of all samples, and the appearance of peaks at approximately 133.2, 154.3, 285.1, 401.2 and 533.1 eV, corresponding to P 2p, S 2p, C 1s, N 1s, and O 1s, respectively. The results suggest that oxygen-, sulfur-, phosphorus- and nitrogen-containing functional groups are present on the carbon surface. The elementary composition of BWC and BWPCs are listed in Table 2. As can be seen, the obtained BWC possesses high contents of N (5.63 at%), O (10.58 at%), S (0.38 at%) and P (0.61 at%) species. For all BWPCs, their

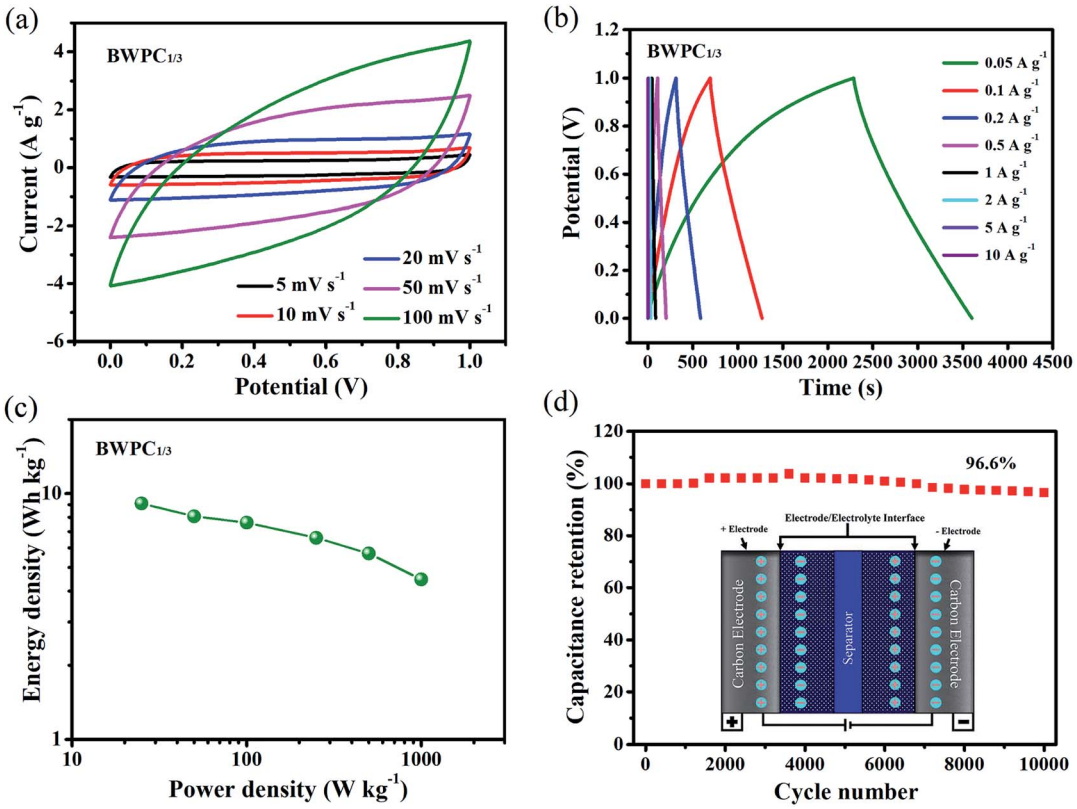

Fig. 7 Electrochemical characteristics of $BWPC_{1/3}$//$BWPC_{1/3}$ symmetric device in 6 M KOH in a two-electrode system: (a) CV curves at different scam rates, (b) GCD curves under different current densities, (c) Ragone plot, (d) cycling stability at 5 A g^{-1} for 10 000 cycles (inset: schematic diagram of the prepared cell-type symmetrical two-electrode supercapacitor).

compositions were found to strongly depend on the KOH dosage, with a high KOH dosage displaying a low heteroatom (N, P and S) doping level. However, it is worth mentioning that the heteroatomic loss is relatively low compared with other biomass-derived carbon materials,[42] which indicate stable heteroatoms doping on the carbon framework of BW. Besides, the oxygen atomic percentage of the BWPCs gradually increases with the increased usage of KOH, owing to the reactions between BW and KOH, which introduces extra oxygen derived from the activator.[38,44]

The C 1s core level spectrum in Fig. 4b, S4b, g and l† show that BWC and BWPCs have two types of C atoms, C=C (284.8 eV) and C–O/C–N (286.1 eV) groups.[45] The N 1s spectra are identified as having four types of chemical states including pyridinic nitrogen (N-6, 397.9 eV), pyrrolic nitrogen (N-5, 399.1 eV), graphitic nitrogen (N-Q, 400.4 eV), and pyridinic nitrogen oxide (N-X, 401.9 eV) (Fig. 4c, S4c, h and m†).[7] The detailed distribution of nitrogen functional groups is further illustrated in Table S1.† It is clear that N-Q represent the dominated species (50–75%). As previously reported,[11,46,47] the N-Q group in carbon materials is helpful for improving the speed of electronic transmission and enhancing the conductivity. While N-5 and N-6 can participate in reversible faradaic reactions and provide extra pseudocapacitance due to its electron-donor property. Therefore, the relatively better electrochemical performances of BWPCs can be expected.

The O 1s peak can be fitted into three different peaks (Fig. 4d, S4d, i and m†), which are associated with C=O including quinones and non-bridging oxygen in the phosphate groups (P=O) (531.1 eV), oxygen single bonded to carbon in C–O and C–O–P groups (532.8 eV), and carboxylic groups (–COOH).[48] It is widely believed that some oxygen species, such as carboxylic groups can also contribute to the pseudo-capacitance *via* reversible redox reactions. To be specific, the pseudo-capacitance of nitrogen and oxygen groups in a basic electrolyte may result from the following reactions:[49,50]

$$C^*H\text{–}NH_2 + 2OH^- \leftrightharpoons C^*{=}NH + 2H_2O + 2e^-$$

$$C^*H\text{–}NH_2 + 2OH^- \leftrightharpoons C^*\text{–}NHOH + H_2O + 2e^-$$

$$\text{–}C{=}O + OH^- \leftrightharpoons \text{–}COOH + e^-$$

$$\text{–}C{=}OOH + OH^- \leftrightharpoons \text{–}C{=}O\text{–}O^- + H_2O$$

Here, C* represents the carbon skeleton.

The peak at 168.8 eV can be ascribed to the oxidized sulfur species (S-1), for instance, the sulfate (–C–SO_4–C–) or sulfonate (–C–SO_3–C–). The peaks at 164.6 and 163.5 eV belong to the S $2p_{1/2}$ (S-2) and S $2p_{3/2}$ (S-3) of the –C–S–C– covalent bond, respectively (Fig. 4f).[34,51] As mentioned above, the presence of sulfur species on the surface of carbon materials can act as electron donor to enhance the electrochemical conductivity,

and ameliorate the surface/interface accessibility to facilitate the infiltration of electrolytes. Furthermore, these groups can function as electrochemically active sites, which play a significant role in boosting pseudo-faradaic reactions of electrode materials.[16,49,51] Interestingly, some phosphorus-containing functional groups are also present in the composition of BW,[52] which results that BWC and BWPCs are doped with phosphorus. The structure of the P 2p peak (Fig. 4e) points to the presence of two major phosphorus groups by their binding energies: pentavalent tetra coordinated phosphate (PO_4, 133.2 eV) and pyrophosphate groups ($(PO_3)_n$, 134.1 eV).[53,54] More details about the XPS analyses can be found in Fig. S4 and Table S1.†

The Nyquist plots of EIS test for all synthesized samples are presented in Fig. 5a. Both BWC and BWPCs show a near-vertical curve at low frequency, demonstrating an ideal capacitive behavior.[47] The *x*-intercept of the semicircle represents the equivalent series resistance (R_s), and the diameter of the semicircle corresponds to the charge-transfer resistance (R_{ct}). The equivalent circuits and fitted curves are depicted in Fig. S5e† and the inset of Fig. 5a. As can be observed, all samples exhibit low R_s of <1.0 Ω. The N, O, S and P elements existing on the surface of carbon material could improve the wettability of samples to electrolytes, which are responsible for the low R_s.[21] Remarkably, $BWPC_{1/3}$ electrode exhibits smaller R_s (0.76 Ω) and R_{ct} (3.11 Ω) value than that of BWC (0.87 and 22.01 Ω), $BWPC_{1/4}$ (0.81 and 7.75 Ω) and $BWPC_{1/2}$ (0.84 and 5.46 Ω) (Table S2†), suggesting its relatively higher electrolyte ion transport rate and good conductivity.

Fig. 5b presents the CV curves of BWPCs-based electrodes with sweep speed of 50 mV s^{-1} with slight distorted typical rectangular shape. Especially, $BWPC_{1/3}$ showed the largest integral area and the closest to the rectangular shape, indicating the best capacitance performance.[11] The slight distortion with faradaic humps resulted from redox reactions can be clearly observed in the CV profiles, which was potentially related to the coexistence of double-layer capacitance from charge accommodation and pseudo-capacitance from N/O/P/S functionalities groups.[47,55] The CV curves of $BWPC_{1/3}$ with diverse sweep speed from 5 to 100 mV s^{-1} are exhibited in Fig. 5c. Even at a high sweep speed of 100 mV s^{-1}, all curves still kept approximately rectangular shape, indicating a good performance with high reversibility. Besides, the CV curves at different scan rates for $BWPC_{1/4}$ and $BWPC_{1/2}$-based supercapacitors are also collected in Fig. S5a and c.†

The GCD curves of BWPCs-based electrodes are illustrated in Fig. 5d. All the GCD curves exhibit approximate symmetric triangle shapes, which reveal nearly ideal capacitive characteristics. The specific capacitance (C_s, F g^{-1}) of $BWPC_{1/4}$, $BWPC_{1/3}$ and $BWPC_{1/2}$-based electrodes are calculated to 221.4, 313.8, and 242.1 F g^{-1} respectively at 1 A g^{-1}. The high C_s of $BWPC_{1/3}$ can be ascribed to the high heteroatomic content, and hierarchical pore distribution with largest S_{BET} and abundant micropores. Besides, the small *IR* drop further demonstrating the low R_s of BWPCs.[56] Fig. 5e shows the GCD curves of $BWPC_{1/3}$ at current density from 0.1 to 10 A g^{-1}. It can be seen that the $BWPC_{1/3}$ exhibits an excellent C_s as high as 371.8 F g^{-1} at a current density of 0.1 A g^{-1}. The superior electrochemical performance of $BWPC_{1/3}$ is also comparable to or much better than many other biomass-derived porous carbons prepared by the KOH activation method (Table 3). Moreover, upon increasing the current density to 10 A g^{-1}, $BWPC_{1/3}$ exhibits high capacitance retention (59.6%), which is higher than that of $BWPC_{1/4}$ (53.2%) and $BWPC_{1/2}$ (54.3%) (Fig. 5f).

To further investigate the practical application of $BWPC_{1/3}$, a two-electrode symmetric device was assembled by using two identical $BWPC_{1/3}$ electrodes (denoted as $BWPC_{1/3}$//$BWPC_{1/3}$). The working potential range of $BWPC_{1/3}$//$BWPC_{1/3}$ symmetric device was firstly investigated by CV curves at 50 mV s^{-1} using 1 M Na_2SO_4 as the electrolyte (Fig. 6a). All CV curves pose reversible cycle with quasi-rectangular shape, even the cell voltage reached up to 2.0 V. Such the high voltage window of $BWPC_{1/3}$//$BWPC_{1/3}$ symmetric device can be ascribed to the high over-potential for dihydrogen evolution caused by the oxygen-containing functional groups in the carbon materials.[61]

The CV curves shown in Fig. 6b exhibit ideal rectangular-shapes with the scan rates increasing from 5 to 100 mV s^{-1}. Furthermore, GCD measurements of the $BWPC_{1/3}$ were conducted with different current densities (Fig. 6c). Even at a low current density of 0.2 A g^{-1}, the GCD curves display the quasi-triangle shape with excellent symmetry, implying an excellent EDLC behavior with good electrochemical reversibility. Based on the discharge curve in Fig. 6c and eqn (2), the C_g of the device was calculated to be 49.5 F g^{-1} at the current density of 0.2 A g^{-1}.

The Ragone plot of between energy density and power density of $BWPC_{1/3}$//$BWPC_{1/3}$ was shown in Fig. 6d. It can be observed that the device delivered an energy density as high as 27.5 W h kg^{-1} at a power density of 200 W kg^{-1}, while an energy density of up to 10.8 W h kg^{-1} was remained at a higher power density of 10 kW kg^{-1}. It is worth noting that such high values for energy densities are superior to the commercial carbon supercapacitors (4 to 5 W h kg^{-1}) and the Partnership for a New Generation of Vehicles power target (~15 kW kg^{-1}).[62]

To investigate the long-term durability of $BWPC_{1/3}$, the cyclic performance was measured using a charge/discharge test at 10 A g^{-1}. The capacitance of the $BWPC_{1/3}$ electrode showed no obvious decay during the cycling process, as depicted in Fig. 6e. After 10 000 cycles, 97.1% of the capacitance was retained in contrast to its initial value, indicating superb cycle performance of the electrode.

The electrochemical performances of $BWPC_{1/3}$//$BWPC_{1/3}$ symmetric devices were further investigated in 6 M KOH electrolyte. Fig. 7a shows the CV curves at different sweep rates. It is obvious that the shapes of all CV curves were approximate rectangles even at a high scan rate of 100 mV s^{-1}, suggesting the highly reversible characteristic of capacitor.

The GCD curves, as shown in Fig. 7b, remain mostly linear and symmetrical in all current densities, further confirming the excellent electrochemical reversibility and ideal double-layer capacitance. The C_g was calculated to be 65.7 F g^{-1}, 58.2 F g^{-1}, 54.8 F g^{-1}, 47.5 F g^{-1} and 41.1 F g^{-1} at 0.05 A g^{-1}, 0.1 A g^{-1}, 0.2 A g^{-1}, 0.5 A g^{-1} and 1 A g^{-1}, respectively.

More importantly, the specific energy density for $BWPC_{1/3}$//$BWPC_{1/3}$ supercapacitor is as high as 9.1 W h kg^{-1} at the power density of 25 W kg^{-1} (Fig. 7c). The cycle stability of $BWPC_{1/3}$ was also investigated in 6 M KOH and the resultant plots are shown in Fig. 7d. As can be seen, 96.6% of its initial capacitance can be remained over 10 000 cycles at the current density of 5 A g^{-1}, confirming its good cyclic stability of the BW-based carbons.

4 Conclusions

In brief, the N–O–P–S co-doping HPCs have been successfully synthesized from bean worm through an efficient yet cost-effective strategy. The results indicate the dosage of KOH has a significant influence on the properties of porous carbon. The multi-heteroatom-doped HPC yielded with the optimum weight ratio of 3 : 1 (BW : KOH) was found to be the best electrode material, which exhibited an impressive S_{BET} of 1967.1 m^2 g^{-1} and proper levels of N–O–S–P heteroatom dopants. When employed in supercapacitor, the specific capacitance of $BWPC_{1/3}$ reaches up to 371.8 F g^{-1} in 6 M KOH solution. Meanwhile, the assembled symmetric device in 1 M Na_2SO_4 delivered the high energy density of 27.5 W h kg^{-1} to afford the power density of 200 W kg^{-1} (an extended voltage window of 2.0 V). The promising performance of N/O/S/P co-doped porous carbon together with the facile fabrication process may hold considerable potential to be applied in large-scale production of high-performance electrode materials for supercapacitors.

Conflicts of interest

There are no conflicts to declare.

Acknowledgements

This work was supported by the university-level platform project of Suzhou University (2019ykf07, 2019ykf05), the undergraduate scientific research project of Suzhou University (KYLXYBXM20-001), Natural Science Research Project of the Education Department of Anhui Province (KJ2019A0671), the Provincial of Natural Science Foundation of Anhui (2008085QB77), Professor (doctor) of Suzhou University Scientific Research Foundation Project (2019jb02), Important Projects of Natural Science Research in Colleges and Universities of Anhui Province in 2017 (KJ2017A435), and Horizontal Research Project of Suzhou University (2020xhx017).

References

1 Z. H. Bi, Q. Q. Kong, Y. F. Cao, G. H. Sun, F. Y. Su, X. X. Wei, X. M. Li, A. Ahmad, L. J. Xie and C. M. Chen, *J. Mater. Chem. A*, 2019, 7, 16028–16045.

2 W. Raza, F. Ali, N. Raza, Y. W. Luo, K. Kim, J. H. Yang, S. Kumar, A. Mehmood and E. E. Kwon, *Nano Energy*, 2018, **52**, 441–473.

3 W. Q. Tian, Q. M. Gao, L. M. Zhang, C. X. Yang, Z. Y. Li, Y. L. Tan, W. W. Qian and H. Zhang, *J. Mater. Chem. A*, 2016, **4**, 8690–8699.

4 S. Zhu, J. F. Ni and Y. Li, *Nano Res.*, 2020, **13**, 1825–1841.

5 S. R. Mangisetti, K. M and S. Ramaprabhu, *Electrochim. Acta*, 2019, **305**, 264–277.

6 Q. H. Geng, G. X. Huang, Y. B. Liu, Y. Y. Li, L. H. Liu, X. H. Yang, Q. Wang and C. X. Zhang, *Electrochim. Acta*, 2019, **298**, 1–13.

7 L. Guan, L. Pan, T. Y. Peng, C. Gao, W. N. Zhao, Z. X. Yang, H. Hu and M. B. Wu, *ACS Sustainable Chem. Eng.*, 2019, **7**, 8405–8412.

8 W. Sun, S. M. Stephen, C. Swartz, D. Williams and F. Q. Yang, *Carbon*, 2016, **103**, 181–192.

9 S. Zhong, M. Kitta and Q. Xu, *Chem.–Asian J.*, 2019, **14**, 3583–3589.

10 X. Jiang, C. Liu, G. F. Shi, G. Y. Wang, Z. Wang, S. M. Jia, Y. C. Dong, P. Mishra, H. Q. Tian and Y. R. Liu, *RSC Adv.*, 2019, **9**, 23324–23333.

11 Q. F. Yao, H. W. Wang, C. Wang, C. D. Jin and Q. F. Sun, *ACS Sustainable Chem. Eng.*, 2018, **6**, 4695–4704.

12 G. Y. Zhao, C. Chen, D. F. Yu, L. Sun, C. H. Yang, H. Zhang, Y. Sun, F. Besenbacher and M. Yu, *Nano Energy*, 2018, **47**, 547–555.

13 G. X. Huang, Q. H. Geng, B. L. Xing, Y. B. Liu, Y. Y. Li, Q. R. Liu, J. B. Jia, L. J. Chen and C. X. Zhang, *J. Power Sources*, 2020, **449**, 227506.

14 G. X. Huang, Q. H. Geng, W. W. Kang, Y. B. Liu, Y. Y. Li, B. L. Xing, Q. R. Liu and C. X. Zhang, *Microporous Mesoporous Mater.*, 2019, **288**, 109576.

15 X. Y. Qian, L. Miao, J. X. Jiang, G. C. Ping, W. Xiong, Y. K. Lv, Y. F. Liu, L. H. Gan, D. Z. Zhu and M. X. Liu, *Chem. Eng. J.*, 2020, **388**, 124208.

16 H. H. Lu, C. Yang, J. Chen, J. Li, H. L. Jin, J. C. Wang and S. Wang, *Small*, 2020, **16**, 1906584.

17 S. M. Zhu, X. F. Dong, H. Huang and M. Qi, *J. Power Sources*, 2020, **459**, 228104.

18 Z. Shang, X. Y. An, H. Zhang, M. X. Shen, F. Baker, Y. X. Liu, L. Q. Liu, J. Yang, H. B. Cao, Q. l. Xu, H. B. Liu and Y. H. Ni, *Carbon*, 2020, **161**, 62–70.

19 Y. L. Wang, B. B. Yang, D. Y. Zhang, H. Shi, M. Lei, H. X. Li and K. J. Wang, *Appl. Surf. Sci.*, 2020, **512**, 145711.

20 X. P. Xin, H. Q. Kang, J. G. Feng, L. N. Sui, H. Z. Dong, P. Zhao, B. L. Pang, Y. J. Chen, Q. Sun, S. Ma, R. F. Zhang, L. F. Dong and L. Y. Yu, *Chem. Eng. J.*, 2020, **393**, 124710.

21 Y. J. Ma, X. G. Zhang, Z. Liang, C. L. Wang, Y. Sui, B. Zheng, Y. C. Ye, W. J. Ma, Q. Zhao and C. L. Qin, *Electrochim. Acta*, 2020, **337**, 135800.

22 Q. Abbas, R. Raza, I. Shabbir and A. Olabi, *Journal of Science: Advanced Materials and Devices*, 2019, **4**, 341–352.

23 L. Sun, H. Zhou, L. Li, Y. Yao, H. N. Qu, C. L. Zhang, S. H. Liu and Y. M. Zhou, *ACS Appl. Mater. Interfaces*, 2017, **9**, 26088–26095.

24 J. Yan, J. Shen, L. Li, X. K. Ma, J. H. Cui, L. Z. Wang and Y. Zhang, *Diamond Relat. Mater.*, 2020, **102**, 107693.

25 X. Q. Zhu, S. Yu, K. T. Xu, Y. Zhang, L. M. Zhang, G. B. Lou, Y. T. Wu, E. H. Zhu, H. Chen, Z. H. Shen, B. F. Bao and S. Y. Fu, *Chem. Eng. Sci.*, 2018, **181**, 36–45.

26 Y. W. Zhu, S. Murali, M. D. Stoller, K. J. Ganesh, W. W. Cai, P. J. Ferreira, A. Pirkle, R. M. Wallace, K. A. Cychosz,

M. Thommes, D. Su, E. A. Stach and R. S. Ruoff, *Science*, 2011, **332**, 1537–1541.
27 Z. L. Liu, D. Tian, F. Shen, P. C. Nnanna, J. G. Hu, Y. M. Zeng, G. Yang, J. S. He and S. H. Deng, *J. Power Sources*, 2020, **458**, 228057.
28 N. F. Sylla, N. M. Ndiaye, B. D. Ngom, B. K. Mutuma, D. Momodu, M. Chaker and N. Manyala, *J. Colloid Interface Sci.*, 2020, **569**, 332–345.
29 F. Ma, S. L. Ding, H. J. Ren and Y. H. Liu, *RSC Adv.*, 2019, **9**, 2474–2483.
30 C. H. Wang, W. W. Wen, H. C. Hsu and B. Yao, *Adv. Powder Technol.*, 2016, **27**, 1387–1395.
31 D. Rathi, D. Gayen, S. Gayali, S. Chakraborty and N. Chakraborty, *Proteomics*, 2016, **16**, 310–327.
32 Q. Li, X. Z. Wu, Y. Zhao, Z. C. Miao, L. B. Xing, J. Zhou, J. P. Zhao and S. P. Zhuo, *ChemElectroChem*, 2018, **5**, 1606–1614.
33 G. X. Lin, R. G. Ma, Y. Zhou, Q. Liu, X. P. Dong and J. C. Wang, *Electrochim. Acta*, 2018, **261**, 49–57.
34 G. Y. Xu, J. P. Han, B. Ding, P. Nie, J. Pan, H. Dou, H. S. Li and X. G. Zhang, *Green Chem.*, 2015, **17**, 1668–1674.
35 M. Y. Song, Y. H. Zhou, X. Ren, J. F. Wan, Y. Y. Du, G. Wu and F. W. Ma, *J. Colloid Interface Sci.*, 2019, **535**, 276–286.
36 S. Yang, S. L. Wang, X. Liu and L. Li, *Carbon*, 2019, **147**, 540–549.
37 H. F. Lin, F. Z. Wu, S. G. Li, Z. H. Liu and W. K. Wang, *J. Econ. Anim.*, 2005, **9**, 177–180.
38 H. Zhang, X. L. Zhou, L. M. Shao, F. Lv and P. J. He, *ACS Sustainable Chem. Eng.*, 2019, **7**, 3801–3810.
39 J. Niu, R. Shao, J. J. Liang, M. L. Dou, Z. L. Li, Y. Q. Huang and F. Wang, *Nano Energy*, 2017, **36**, 322–330.
40 C. Quan, R. R. Su and N. B. Gao, *Int. J. Energy Res.*, 2020, **44**, 4335–4351.
41 P. Cheng, S. Y. Gao, P. Y. Zang, X. F. Yang, Y. L. Bai, H. Xu, Z. H. Liu and Z. B. Lei, *Carbon*, 2015, **93**, 315–324.
42 J. Song, W. Z. Shen, J. G. Wang and W. B. Fan, *ChemElectroChem*, 2018, **5**, 1451–1458.
43 X. L. Su, J. R. Chen, G. P. Zheng, J. H. Yang, X. X. Guan, P. Liu and X. C. Zheng, *Appl. Surf. Sci.*, 2018, **436**, 327–336.
44 Y. L. Wang, Q. L. Qu, S. T. Gao, G. S. Tang, K. M. Liu, S. J. He and C. B. Huang, *Carbon*, 2019, **155**, 706–726.
45 D. Y. Tang, Y. Y. Luo, W. D. Lei, Q. Xiang, W. Ren, W. C. Song, K. Chen and J. Sun, *Appl. Surf. Sci.*, 2018, **462**, 862–871.
46 Y. Liu, L. J. Cao, J. Luo, Y. Y. Peng, Q. Ji, J. Y. Dai, J. Zhu and X. Q. Liu, *ACS Sustainable Chem. Eng.*, 2019, **7**, 2763–2773.
47 L. Wan, X. Li, N. Li, M. J. Xie, C. Du, Y. Zhang and J. Chen, *J. Alloys Compd.*, 2019, **790**, 760–771.
48 X. D. Yan, Y. H. Yu and X. P. Yang, *RSC Adv.*, 2014, **4**, 24986–24990.
49 L. Wan, W. Wei, M. J. Xie, Y. Zhang, X. Li, R. Xiao, J. Chen and C. Du, *Electrochim. Acta*, 2019, **311**, 72–82.
50 D. H. Wang, Y. Z. Wang, Y. Chen, W. Liu, H. Q. Wang, P. H. Zhao, Y. Li, J. F. Zhang, Y. G. Dong, S. L. Hu and J. L. Yang, *Electrochim. Acta*, 2018, **283**, 132–140.
51 S. Jia, J. Wei, X. T. Meng and Z. Q. Shao, *Electrochim. Acta*, 2020, **331**, 135338.
52 M. H. Yan, C. M. Lu, G. J. Zhang, H. C. li, X. G. Nie, D. Y. Zheng and X. Zheng, *J. Anhui Agric. Sci.*, 2008, **36**, 874–876.
53 J. T. Jin, X. C. Qiao, F. Zhou, Z. S. Wu, L. F. Cui and H. B. Fan, *ACS Appl. Mater. Interfaces*, 2017, **9**, 17317–17325.
54 D. Hulicova-Jurcakova, A. M. Puziy, O. L. Poddubnaya, F. Suárez-García, J. M. D. Tascón and G. Q. Lu, *J. Am. Chem. Soc.*, 2009, **131**, 5026–5027.
55 D. X. Guo, X. M. Song, B. N. Li, L. C. Tan, H. Y. Ma, H. J. Pang, X. M. Wang, L. L. Zhang and D. W. Chu, *J. Electroanal. Chem.*, 2019, **855**, 113349.
56 W. Du, X. N. Wang, X. Q. Sun, J. Zhan, H. D. Zhang and X. J. Zhao, *J. Electroanal. Chem.*, 2018, **827**, 213–220.
57 G. G. Huang, Y. Wang, T. Y. Zhang, X. X. Wu and J. J. Cai, *J. Taiwan Inst. Chem. Eng.*, 2019, **96**, 672–680.
58 K. Y. Perez-Salcedo, S. Ruan, J. Su, X. Shi, A. M. Kannan and B. Escobar, *J. Porous Mater.*, 2020, **27**, 959–969.
59 S. J. Meng, Z. L. Mo, Z. L. Li, R. B. Guo and N. J. Liu, *Mater. Chem. Phys.*, 2020, **246**, 122830.
60 W. J. Lu, X. H. Cao, L. N. Hao, Y. P. Zhou and Y. W. Wang, *Mater. Lett.*, 2020, **264**, 127339.
61 Y. F. Cheng, B. Q. Li, Y. J. Huang, Y. M. Wang, J. C. Chen, D. Q. Wei, Y. J. Feng, D. C. Jia and Y. Zhou, *Appl. Surf. Sci.*, 2018, **439**, 712–723.
62 X. Y. Chen, C. Chen, Z. Zhang, D. H. Xie, X. Deng and J. W. Liu, *J. Power Sources*, 2013, **230**, 50–58.

